# Design and Testing of a Morphing Wing for an Experimental UAV

**P. Gamboa**
Universidade da Beira Interior
6200-358 Covilhã
Portugal

**P. Aleixo, J. Vale, F. Lau**
IDMEC - Instituto Superior Tecnico, Lisbon, Portugal

**A. Suleman**
University of Victoria, Victoria, BC, V8W 3P6, Canada

## *ABSTRACT*

*A morphing concept for wing drag reduction for a small UAV is presented. The results of a computational assessment of the morphing concept benefits are shown. 14% to 30% drag reduction in different flight stages serve as motivation for the construction of a prototype. Design requirements of the morphing mechanism structure are pointed out and constructive solutions are shown. Feasibility and functionality of the constructive solutions are discussed briefly. Wind tunnel test results are not available yet.*

## 1.    INTRODUCTION

The purpose of introducing morphing capability to aircraft wings is to improve aircraft performance at different stages of flight.

Performance parameters that can be improved are, among others, maximum speed, fuel consumption, manoeuvrability, payload, range, endurance, stability and so on. Improving some or all of these parameters would increase efficiency of flight, thus widening the possible mission profiles that the aircraft can perform.

Improvement of the performance parameters can be achieved by changing the aircraft shape, especially the wing planform and airfoil shapes. Changing wing planform means varying a number of geometrical parameters such as span, chord length, sweep angle, dihedral angle and wing twist while airfoil shape change can be achieved by varying parameters like maximum relative thickness and camber line curvature.

Many studies on morphing wing concepts have been performed with small scale models that allow changes in one or more of these geometrical parameters. Studies on flexible wings allowing complex wing shapes have been performed in the University of Florida [1] in micro air vehicles. Gull-wing studies for stability improvement [2] and segmented wings for lift-to-drag ratio improvement [3] have been carried out at the same university. Hyper-elliptic wings [4] allow area increase while attempting to reduce drag through Oswald coefficient improvement caused by the dihedral angle change, while inflatable wings [5] actuated by piezoelectric actuators try to reduce wing weight and alter the camber line through the use of conformal flaps [6]. Variable cant angle winglets [7] and variable span wing [8] research has also been made.

# Report Documentation Page

*Form Approved*
*OMB No. 0704-0188*

Public reporting burden for the collection of information is estimated to average 1 hour per response, including the time for reviewing instructions, searching existing data sources, gathering and maintaining the data needed, and completing and reviewing the collection of information. Send comments regarding this burden estimate or any other aspect of this collection of information, including suggestions for reducing this burden, to Washington Headquarters Services, Directorate for Information Operations and Reports, 1215 Jefferson Davis Highway, Suite 1204, Arlington VA 22202-4302. Respondents should be aware that notwithstanding any other provision of law, no person shall be subject to a penalty for failing to comply with a collection of information if it does not display a currently valid OMB control number.

| 1. REPORT DATE | 2. REPORT TYPE | 3. DATES COVERED |
|---|---|---|
| **01 NOV 2007** | **N/A** | **-** |

| 4. TITLE AND SUBTITLE | 5a. CONTRACT NUMBER |
|---|---|
| **Design and Testing of a Morphing Wing for an Experimental UAV** | 5b. GRANT NUMBER |
| | 5c. PROGRAM ELEMENT NUMBER |
| 6. AUTHOR(S) | 5d. PROJECT NUMBER |
| | 5e. TASK NUMBER |
| | 5f. WORK UNIT NUMBER |

| 7. PERFORMING ORGANIZATION NAME(S) AND ADDRESS(ES) | 8. PERFORMING ORGANIZATION REPORT NUMBER |
|---|---|
| **Universidade da Beira Interior 6200-358 Covilhã Portugal** | |

| 9. SPONSORING/MONITORING AGENCY NAME(S) AND ADDRESS(ES) | 10. SPONSOR/MONITOR'S ACRONYM(S) |
|---|---|
| | 11. SPONSOR/MONITOR'S REPORT NUMBER(S) |

**12. DISTRIBUTION/AVAILABILITY STATEMENT**
**Approved for public release, distribution unlimited**

**13. SUPPLEMENTARY NOTES**
**See also ADM202416., The original document contains color images.**

**14. ABSTRACT**

**15. SUBJECT TERMS**

| 16. SECURITY CLASSIFICATION OF: | | | 17. LIMITATION OF ABSTRACT | 18. NUMBER OF PAGES | 19a. NAME OF RESPONSIBLE PERSON |
|---|---|---|---|---|---|
| a. REPORT **unclassified** | b. ABSTRACT **unclassified** | c. THIS PAGE **unclassified** | **UU** | **30** | |

**Standard Form 298 (Rev. 8-98)**
Prescribed by ANSI Std Z39-18

Optimization processes using CFD algorithms can be used to obtain optimum airfoil and wing planform shapes for one or more performance parameters at different flight conditions [9]. The more realistic the optimization constraints imposed on the design are the better will be the computational assessment of the advantages of introducing a morphing mechanism that can perform such shape changes.

In this paper, we present the motivation, design, construction and testing of a morphing wing with span and chord expansion capability. The morphing wing design is done using aerodynamic shape optimization and a coupled aero-structural analysis. The numerical results of the morphing wing design are compared, in terms of drag performance, to a tested and flown conventional wing fitted to a small UAV, which has been used for active aeroelastic wing research [10]. The numerical results justify the development of a prototype of the wing with a somewhat simpler mechanism to asses its practical implementation and its performance capabilities.

Section 2 briefly presents the results of an optimization process followed by a coupled aerodynamic and structural analysis performed by Gamboa et al. [11] as motivation for the design and construction of a morphing wing with variable span and variable chord capabilities. Section 3 presents the design and construction of a prototype of the morphing wing, as well as the difficulties encountered during the manufacturing of the actuation system and structure. Finally, in section 4 the wind tunnel testing procedure and the aerodynamic test results are discussed.

## 2.  AERODYNAMIC OPTIMIZATION AND COUPLED AERO-STRUCTURAL ANALYSIS RESULTS

The goal of this part of the work is to design a wing that can reconfigure itself in flight in order to improve its performance at a given flight speed. The wing must be designed to fly from 15m/s to 50m/s with reduced drag over the original wing. The flight altitude is kept constant at sea level.

Three steps are required for this design problem: an aerodynamic shape optimization step to provide the optimal wing aerodynamic shapes for the various speeds; a structural model step that creates the wing geometry mesh with the materials used; and a coupled aerodynamic-structural analysis step to determine the final shape of the wing under aerodynamic loading.

### 2.1    Aerodynamic Shape Optimization

The objective of the morphing wing design is to minimize the wing drag, $D_W$, at all speeds when lift, $L$, equals the aircraft weight. In order to achieve this, a tool that searches for the best airfoil geometry and the best wing planform shape, given geometric constraints imposed by the limitations of the morphing technology, is used. The aerodynamic analysis is done in two steps. First, the 2-dimensional (2D) aerodynamic coefficients as functions of angle of attack (AOA) and Reynolds number (*Re*) at specified wing sections across the span are obtained using the solver of the XFOIL code [12]. The airfoils are represented by b-spline control points in a similar fashion as is described in [9] but, instead of using the control points to define the airfoil surface, one uses the control points to define the airfoil camber line and the airfoil thickness distribution. Then, a non-linear lifting-line method [13] algorithm is used to obtain the lift distribution and induced drag. The lift and the parasite drag are obtained by integrating the lift and parasite drag coefficients corresponding to all local angle s of attack. The wing is represented by the chord and incidence at specified sections along the semi-span. The sections' aerodynamic information comes from the previous step. The aerodynamic shape optimization is carried out with the sequential quadratic programming (SQP) constrained optimization algorithm DONLP2 [14]. The gradients of the objective function and constraints are a requirement of any gradient-based optimization algorithm. In this work, the gradients are computed using forward finite-differences. Using finite-differences enables the problem of finding the gradients to be treated as a black box and therefore, it can be used with any fluid flow solver

because it does not involve changes in the solver's code.

A total of 13 design variables are adopted in this design problem. The design variables are the angle of attack, $\alpha$, the span of the wing, $b$, and the chord length, $c$, at two semi-span positions (the chord where the wing joins the central wing and the tip chord) and the airfoil shape. In this case, the span is allowed to vary between 2.4m and 3.4m and the chord length is limited to a minimum of 0.22m and a maximum of 0.33m. The variation of the chord length between these two design chords is linear. The airfoils at the reference stations can change its thickness and camber distributions only limited by a thickness in the range 14mm to 25.2mm. There is no twist of the wing since the morphing concept does not permit such mechanism and the sweep angle at quarter chord position is kept constant and equal to zero. These geometric constraints are imposed due to the physical limitations of the morphing mechanisms and the rubber-like material to be used for the skin. A fixed leading edge diameter, $\phi_{LE}$, is imposed since the morphing mechanism concept does not allow it to be changed.

The aim of the optimization is to minimize the drag of the wing at speeds between 15m/s and 50m/s. The design variables and the constraints are summarized in Table 1.

| Design variable | Constraint | Greater than | Equal to | Less than |
|---|---|---|---|---|
| - | lift, N | - | 100 | - |
| - | leading edge radius, mm | - | 2 | - |
| span, m | - | 2.4 | - | 3.4 |
| root chord, m | - | 0.22 | - | 0.33 |
| tip chord, m | - | 0.22 | - | 0.33 |
| angle of attack, deg | - | - | - | - |
| - | $|z_{(x/c)=0.75}|$, mm | 4 | - | 7.2 |
| - | $|z_{(x/c)=0.5}|$, mm | 6 | - | 10.8 |
| - | $|z_{(x/c)=0.25}|$, mm | 7 | - | 12.6 |
| - | $|z_{(x/c)=0.167}|$, mm | 6 | - | 10.8 |
| - | $|z_{(x/c)=0.083}|$, mm | 5.5 | - | 9.9 |

**Table 1: Design variables and constraints.**

The design variables 5 to 13 are the abcissas of the airfoil's b-spline control points coordinates non-dimensionalized by the chord length. Here, the b-spline is represented by 13 control points from which the points 2 to 6 are used as design variables for the thickness distribution and points 9 to 12 are used for the camber line of the airfoil at $0c$, $0.0833c$, $0.25c$, $0.5c$ and $0.75c$. In this work only the geometry of one airfoil is changed and all wing sections use the same surface $z$ value at the same $x/c$ position, so that all $z$ values are within the limits specified above. The tool allows different airfoils to be designed at different wing stations, but due to the strict geometric constraints and the need for a simple mechanism actuation it was observed that only small drag reductions were achieved, which did not pay-off the increased computational time required and the resulting mechanical complexity.

The initial design was the minimum wing area planform and a representation of the NACA 0009 airfoil which fits the required wing section geometric constraints. The wing semi-span was divided into 50 sections for the lifting-line analysis. A total of 150 panels were used in the airfoil analysis, concentrating the points closer to the small radius leading edge in a cosine distribution. Convergence of the optimization proved to be very dependent on the initial design. It was observed that starting the optimization at higher speeds and using the optimized design at a given speed as the starting point for the next reduced speed helped greatly in the optimization process.

### 2.1.1 Aerodynamic Shape Optimization Results

The optimized geometry of the morphing wing is summarized in Fig. 1. It can be observed that, as speed reduces, the airfoil thickens up and the camber increases with its maximum value moving slightly forward on the chord. The solution at lower speeds was very much restricted by the airfoil geometry constraints. Since the morphing concept has limited capability to increase thickness and camber then, the maximum allowable wing planform area was never attained because, for the maximum chord length, the airfoil becomes so thin (about 6.3% of relative thickness) that its maximum lift coefficient is very low and the extra area is not sufficient to outperform the higher maximum lift coefficient obtained from a slightly thicker airfoil with smaller chord length. From Fig. 1, only below 20m/s does the root chord start to stretch to produce a tapered wing. At 40m/s and above, the wing exhibits its minimum possible planform area.

The drag results are presented in sub-section 2.4 below together with the drag results of the conventional wing and the deformed wing obtained from the aero-structural analysis.

## 2.2 Structural Design

In order to achieve the desired shape changes for the morphing wing, the skin material has to allow high strains, which is not the case with the materials usually used in conventional aircraft. Therefore, rigid materials, as metals or high stiffness/low strain polymer membranes, were ruled out. Rubber materials and other polymers could be considered candidates, including new smart materials as shape memory polymers. Nevertheless, vulcanized rubber was chosen to be the skin material, due to its availability, low price and the desire to prove the feasibility of the morphing concept without much concern about cyclic fatigue or environmental hazard. The use of a shape memory polymer was initially considered, but the increase in complexity of the morphing system due the heating requirements and the elastic-perfectly plastic behaviour of such material makes its shape memory properties at least unusable when the wing is loaded.

The structural model must, not only, be capable of increasing the chord at a wing section but also of discretizing the airfoil and allowing changes in airfoil thickness at some control points. In this work, it is considered that the mechanism divides the airfoil in 6 different sections along the chord, three of them being evenly spaced from the quarter chord to the leading edge and the last three sections being evenly spaced from the quarter chord to the trailing edge. A total of 10 control points are considered for thickness changes, five on the upper surface of the airfoil and five on its lower surface, paired at the same chordwise coordinate. Leading edge and trailing edge points are not considered for thickness changes. As the mechanism expands the chordwise relative positions of the control points is maintained. The span expansion mechanism is intended to stretch the wing skin and also maintain the rib expansion mechanisms evenly distributed along the span of the wing.

The actual mechanism is not important at this stage. What is necessary is that the model allows the control points, the leading edge and the trailing edge to be placed at the chordwise and spanwise positions required by the aerodynamic design optimization results.

### 2.2.1 Wing FEM Structural Model

The finite element method (FEM) structural model of the wing was built not only to perform the coupled aerodynamic-structural analysis but also to assess the wing deformation forces involved in such a structure. Therefore, the model is required to allow the application of aerodynamic loads on the wing deformable skin and stringers and simulate some of the moving parts of the morphing mechanism in such a way that relevant forces and moments acting on it can be obtained.

Rubber like materials can be modelled in a number of ways when a FEM is applied, traditionally, using a strain energy function dependant only on deviatoric deformations. A variety of strain energy functions are supported by Ansys®, the commercial structural analysis program used [15], and the user can choose the

one that better fits the material data that is being modelled.

For simplicity, the parts of the extension mechanisms of the ribs that are not modelled and the spar extension mechanism are assumed to be rigid enough to support all deformation loads with negligible deformation of their own. Later work considered models of the complete mechanisms in order to create a
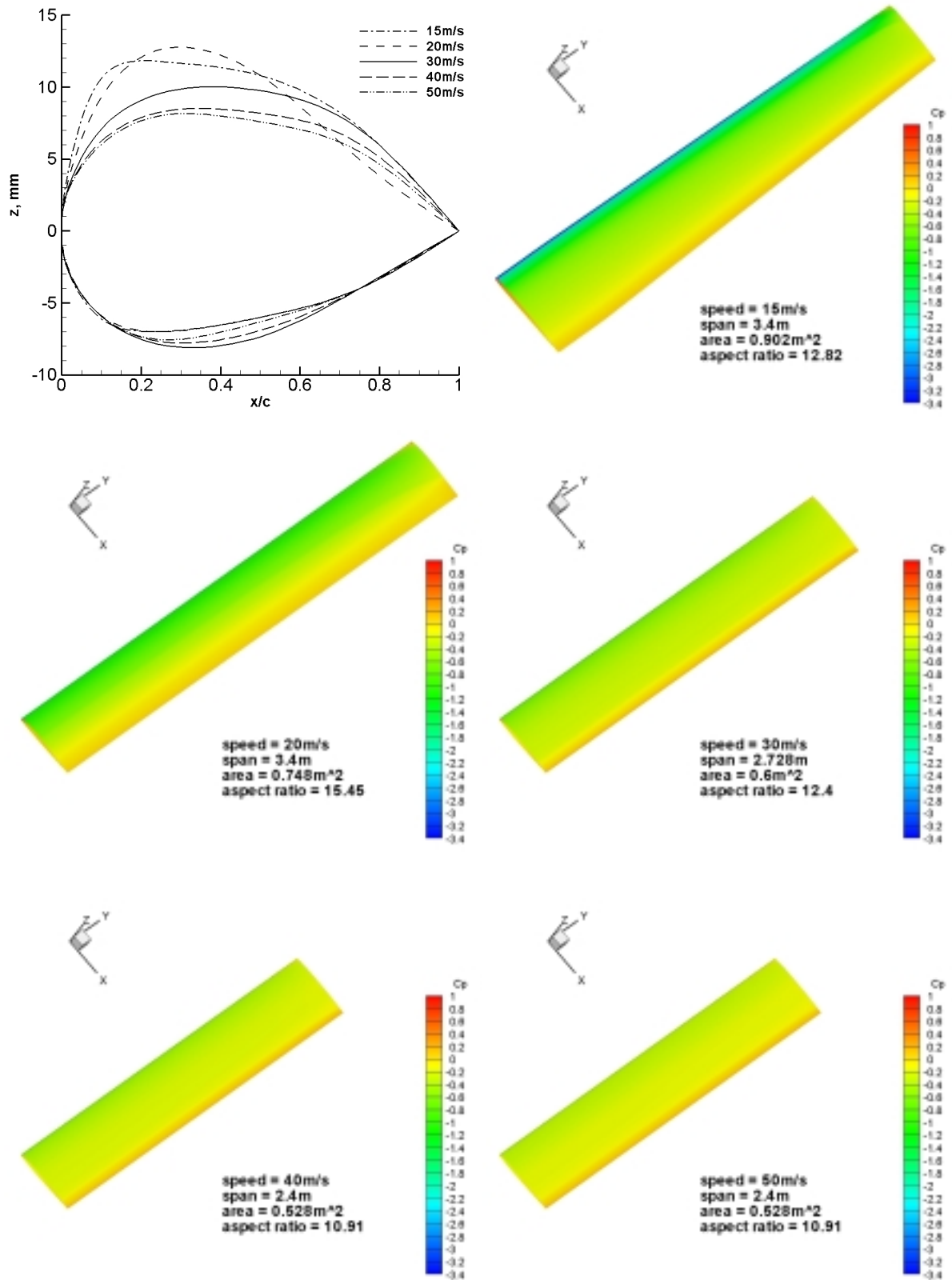
**Figure 1: Airfoil sections and wing planforms for five speeds.**

more realistic model. In order to avoid the use of surface to surface contact elements, some beam components used for skin deformation were modelled as elastic stringers with high Young modulus (see Fig. 2). By doing so, one prevents building a computationally heavy model with convergence difficulties. This is done at the expense of obtaining higher deformation forces than those that are required in reality, since a component which is supposed to slide against the wing skin with negligible friction force is modelled as a stringer that needs to be stretched.

Aerodynamic loads are applied directly to the skin nodes as forces in the Cartesian reference frame. Since the aerodynamic mesh is different from the mesh used for the structural analysis (which is more refined), then forces in a particular location are evenly distributed around the surrounding skin nodes.

A simple convergence study using a section of the wing was performed to assess the suitability of the FEM mesh. This study revealed that the refinement of the mesh could solve convergence problems but deformation forces and moments results did not differ significantly from a less refined mesh to a more refined mesh. Therefore, to reduce computation time requirements the least refined mesh was chosen to be used in the structural analysis and more refined meshes were used whenever convergence problems occurred.

In order to resist and transmit aerodynamic forces to the structure, the wing skin acting as a membrane must be stretched prior to the loading. However, the rubber material model used in this work becomes unstable at high stretches, say higher than 170%, which means that for a fully deformed wing a high initial stretch would cause model convergence problems. Therefore the initial stretch was adjusted to allow the full analysis of the wing for each flight condition, bearing in mind that, real rubber materials can stretch up to 300% and more and that this action will cause error in the prediction of deformation forces.
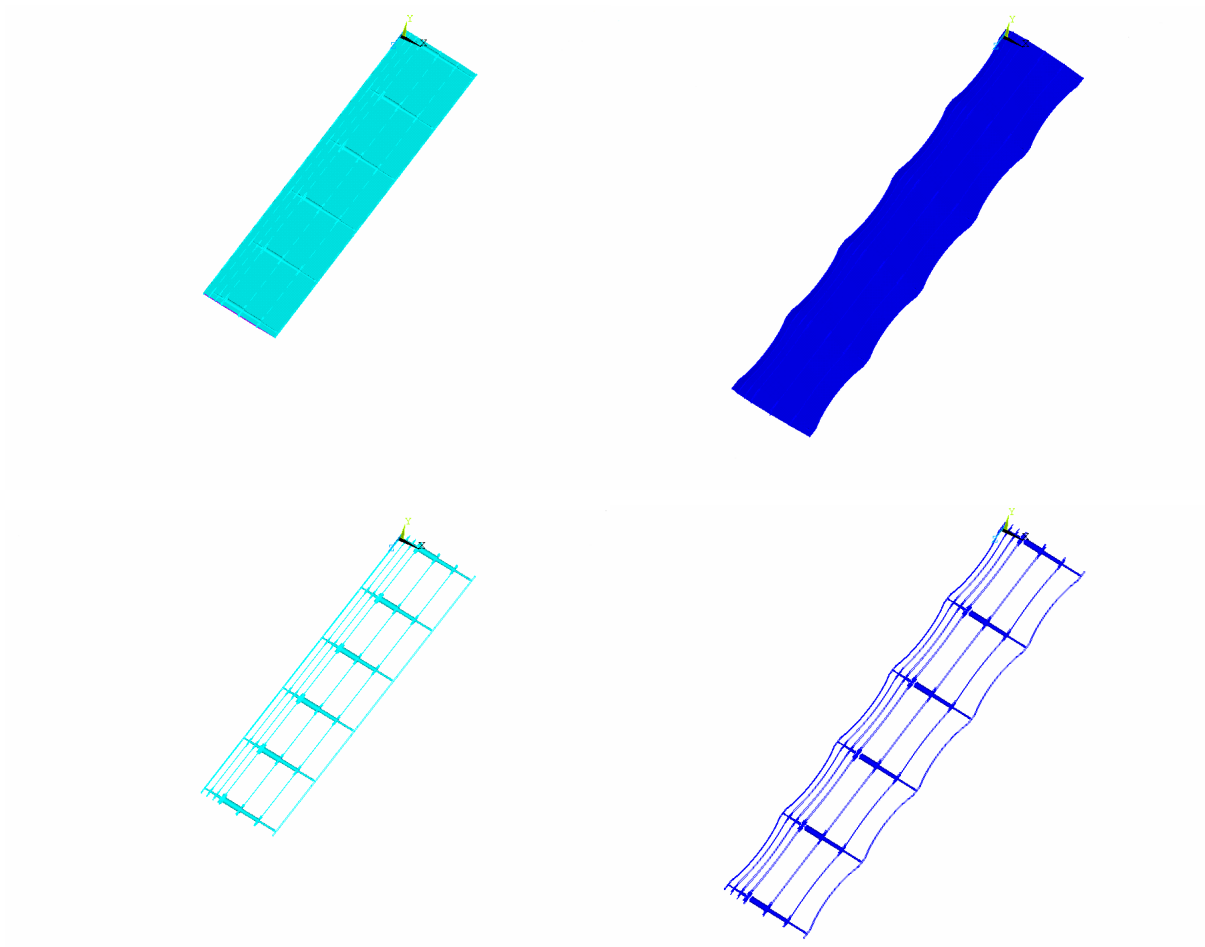
**Figure 2: FEM wing model showing (above) the undeformed and stretched skin and (below) the undeformed and stretched ribs and stringers.**

## 2.3    Coupled Aero-Structural Analysis

The process used to estimate the morphing wing drag and structural requirements is illustrated in Fig. 3. At a given flight condition and aircraft weight, the aerodynamic optimization tool optimizes the wing shape and passes it together with the aerodynamic loads to the structural model. Here the structural control points are made coincident to the aerodynamic control points and the aerodynamic loads are distributed to the skin FEM nodes. Then, the structural analysis is carried out with the control points fixed and de deformations of the skin are obtained. In the next iteration, the new wing shape is passed to the aerodynamic solver and new loads are computed. The process is repeated until convergence is achieved.

The convergence criterion for this coupled problem is based on the aerodynamic loads, because only these loads vary and cause different deformations on the structure. Once the aerodynamic loading is nearly constant after consecutive iterations, the deformed wing has its stationary shape for the current flight condition. Therefore, convergence is assumed when the force variation on each node falls below 1%.
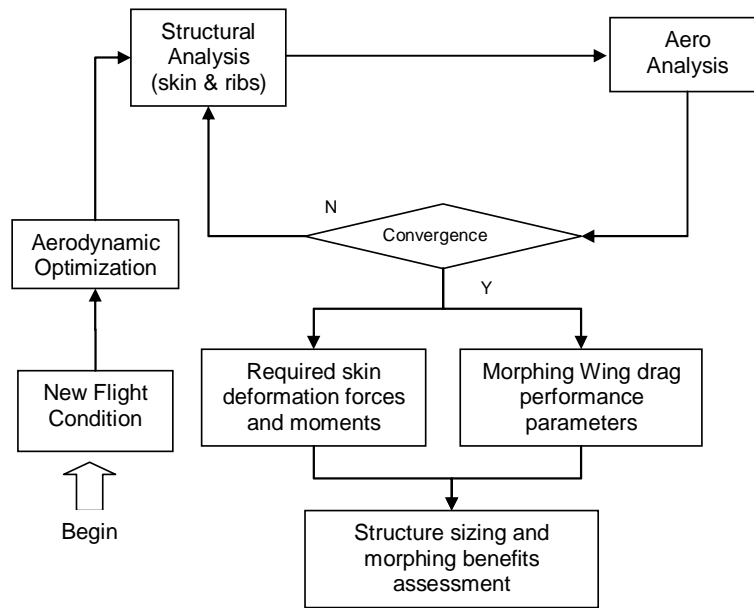
**Figure 3: Flow chart of coupled aero-structural analysis of an optimum morphing wing at different flight speeds.**

### 2.3.1    Coupled Aero-structural Analysis Results

Since rubber is not a rigid material, when it is wrapped as a sleeve around the wing internal mechanism and structure with some level of pre-extension it tends to the shape shown in Fig. 2. Straight lines form between consecutive control points at any section and the chord and thickness reduce between consecutive ribs. As a result, the wing aerodynamic characteristics are different from the perfectly smooth optimized wing. The solution from the aero-structural analysis is shown in Fig. 4.

The depicted airfoils in Fig. 4 are those at the tip of the wing. Clearly shown, is the deformation which results from the suction that exists around the airfoil. Since the control points do not move for a given configuration, the surface of the airfoil exhibits undesired bumps between and at the control points. The pressure coefficient distributions around the wing illustrate the peaks of alternating zones of low pressure and high pressure that occur due to the small curvature of the wing surface at the control points.

The deformation of the chord of the wing also resulted in reduced wing area as can be seen by comparing Fig. 1 with Fig. 4. Wing drag was mainly affected by the section deformation. Induced drag remained almost unchanged.

At the moment a better structural model is being analysed. Improvements have been made to the leading edge curvature in order to better represent the shape obtained from the optimization process. Also, around the control points, where the stringers are fixed, the beam elements used did not represent well the physics of the skin since the elements' rigidity forced the yet unloaded skin to have an arc-like shape between control points. Now, this rigid zone has been reduced to nearly a point to allow the skin to be straight when unloaded.
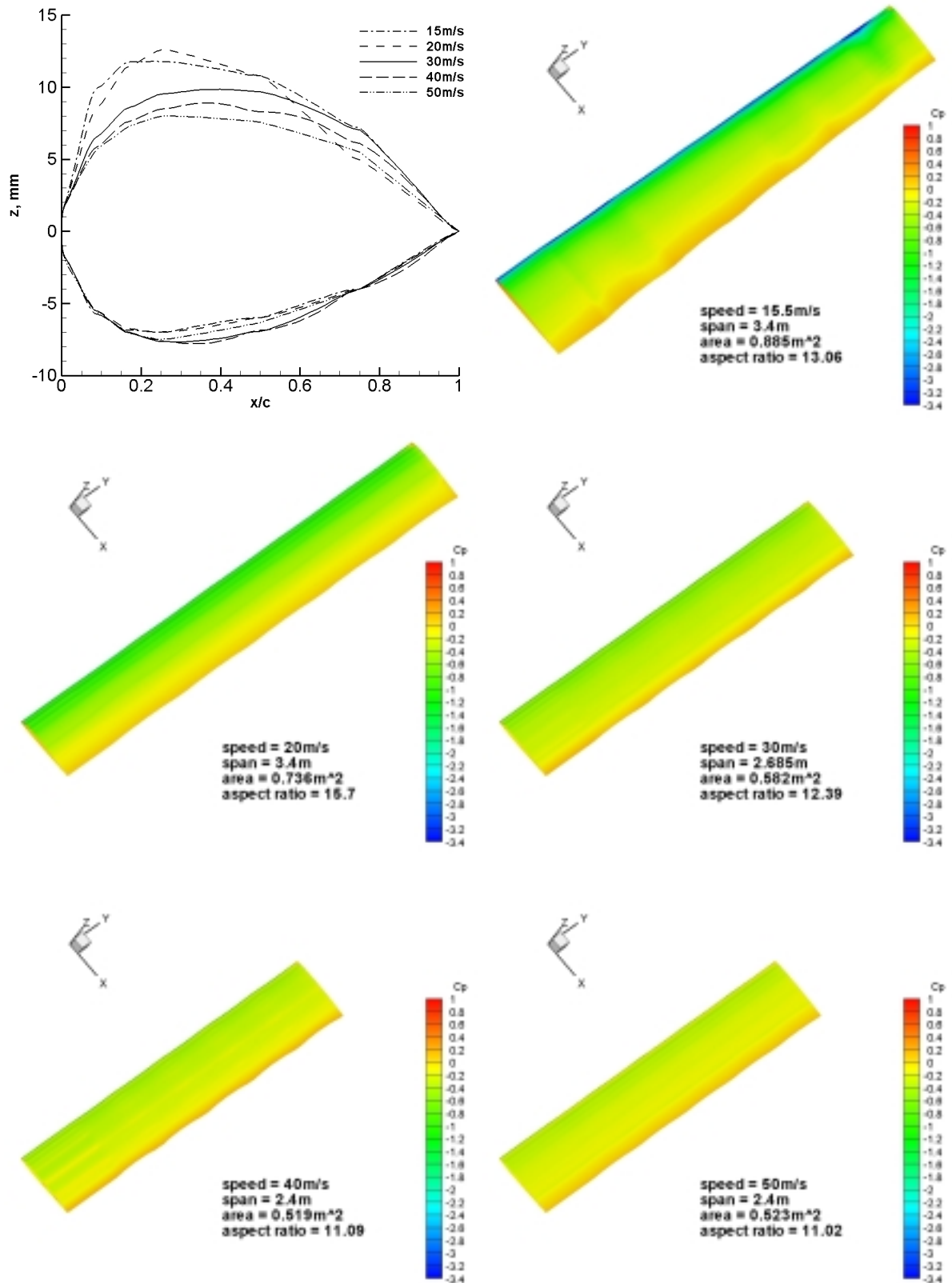
**Figure 4: Airfoil sections at wing tip and wing planforms for five speeds from the aero-structural analysis.**

## 2.4 Wing Drag Results

When comparing the optimized morphing wing with the original wing drastic drag reductions are obtained at all speeds above 14.5m/s. Figure 5 illustrates well this. At the original wing cruise speed of 30m/s, drag has reduced by more than 50%. These large reductions are due to the fact that the original wing, owing to its design requirement of good low speed performance, has the highly cambered FX63-237 airfoil and a large wing area. The morphing wing design, despite its shortcomings at low speed due to the limited thickness and camber that can be produced, can adapt to a wide range of speeds by changing its wing area and airfoil.

As anticipated, the performance of the deformed morphing wing is not so good. The skin surface deformation greatly influenced the parasite drag of this wing. The drag improvements are about half of those of the optimized morphing wing. For instance, at 30m/s the reduction in drag is 22.5%. There is a quite important shortcoming at low speed. Below 17m/s drag is greater than in the original wing and the stall speed increased from 12m/s to 15.5m/s. The optimized morphing wing still manages a stall speed of 14m/s. Table 2 summarizes the percent reductions in drag obtained by the morphing wing.

One important advantage of the morphing wing is that the angle of attack between 25m/s and 50m/s varies only by 1.3deg. This situation helps in maintaining the fuselage in an almost horizontal position for most of the speed range in straight and level flight, which for some surveillance applications may be of interest. On the other hand, fuselage drag can be reduced since it may be at a small angle of attack to the airflow.
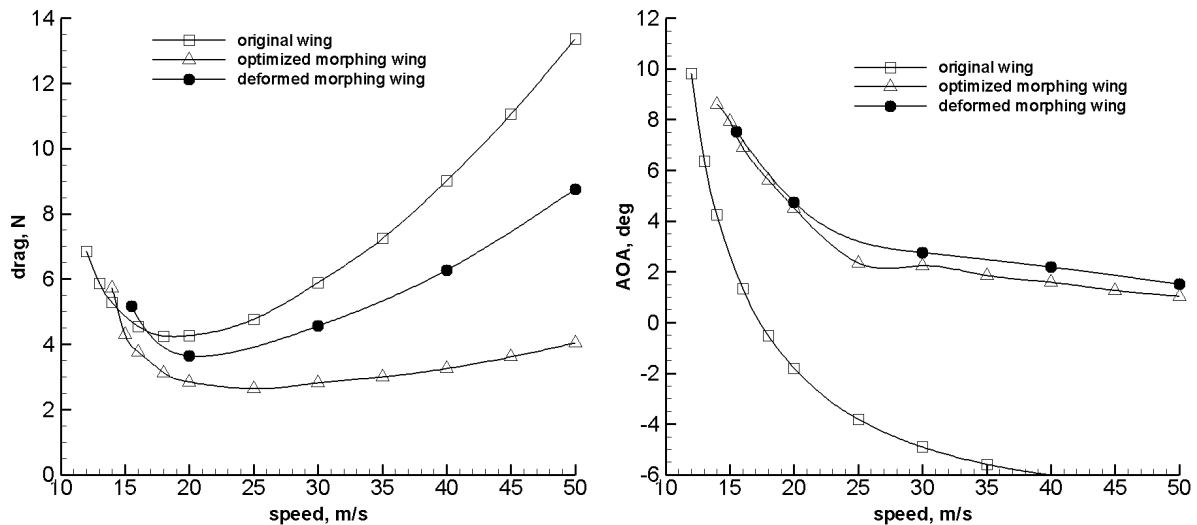


**Figure 5: Comparison of drag and angle of attack estimates of the original wing, the optimized morphing wing and the deformed morphing wing for various flight speeds.**

| Wing | 15m/s | 20m/s | 30m/s | 40m/s | 50m/s |
|---|---|---|---|---|---|
| optimized morphing | 11.2 | 33.3 | 52.2 | 63.9 | 69.7 |
| deformed morphing | -6.3 | 14.7 | 22.5 | 30.4 | 34.5 |

**Table 2: Percent drag reductions with optimized morphing wing and deformed morphing wing.**

### 2.4.1 Morphing Wing Concept Limitations

The limitations imposed by the morphing concept described in this work are concerned with the degree of the approximation to the optimized wing shape that the morphing mechanism is able to comply. The main

differences between the optimized shape and the deformed wing shape consist of:

- • - Straightening of the wing sections between the ribs and consequent loss of wing area;
- • - Inability of the mechanism to provide the ribs with a smooth airfoil shape with curved lines between control points;
- • - The fixed leading edge radius becomes small when, at low speeds, the maximum thickness and camber positions move forward and the first control point stands out creating a good place to trigger separation;
- • - The mechanism limitation in airfoil camber line change, necessary for low speed flight.

The rest of the paper deals with the mechanical design, construction and aerodynamic testing of a small prototype of a morphing wing that changes chord and span. A larger leading edge radius was adopted to avoid premature separation due to poor leading edge geometry.

# 3.     DESIGN AND CONSTRUCTION OF THE MORPHING WING PROTOTYPE

This section describes the design and construction process of the morphing wing prototype. Structural forces and moments that the morphing mechanism is required to withstand were based on the deformation forces and moments obtained from the structural FEM model.

The decision was taken to conceptualize a mechanism that allowed chord and span changes only, trying to approximate all possible wing planforms between the smallest area wing and the maximum area wing. Tapered and elliptical approximations are shown in figure 6.
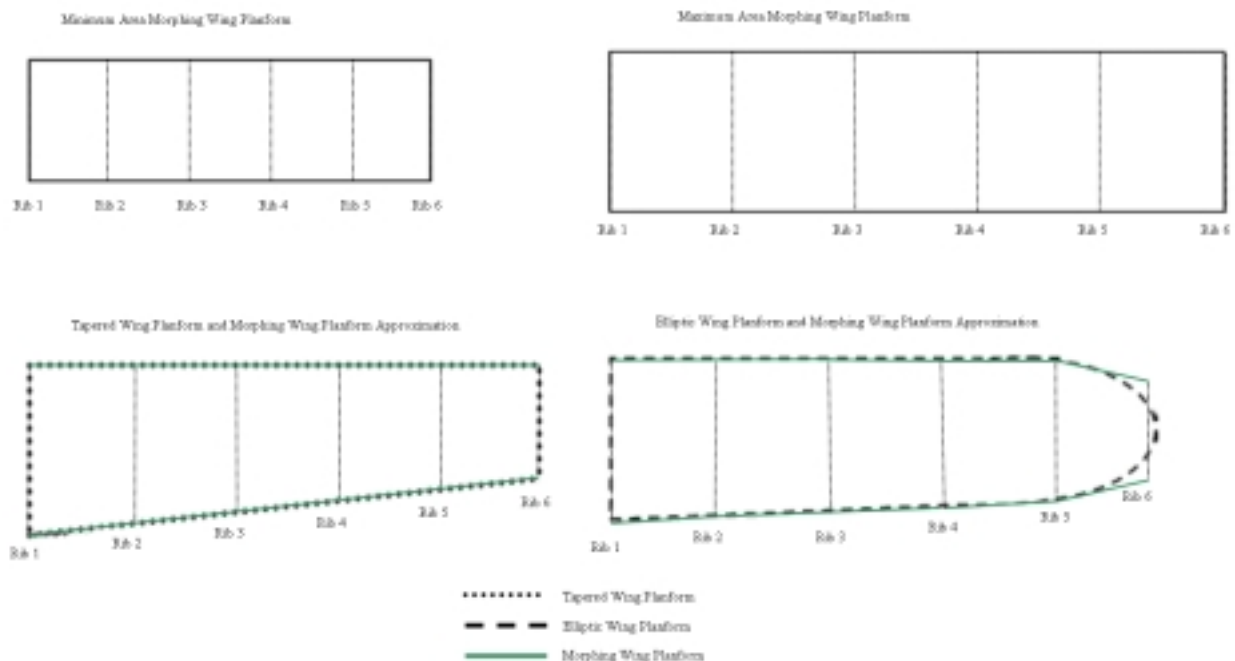


**Figure 6: Morphing Mechanism conceptual capability**

The limits of the span and chord increase were assumed to be 50%, which is safely below the rupture

strain of rubbers under equal biaxial loading [16].

Each chord expansion mechanism is independently actuated to improve the level of freedom in obtaining different planform shapes. Furthermore, independent servos are used to extend the chord in the leading edge direction and trailing edge direction at the rib sections so that the quarter chord line can be made to stay perpendicular to the wing root section.

## 3.1    Morphing Mechanism Design for wind tunnel testing

The structural FEM model produced the following results in terms of forces for a morphing wing with the capabilities described in the previous chapter in its fully extended position:

- Total compressive force in the span direction - 8000N.
- Total compressive force in the chord direction per rib - 1500N.
- Total compressive force in the thickness direction per rib - 250N.

These total forces refer to the full scale half wing, which in its retracted state is 1m long span wise, 0.22m long chord wise and has a 0.002m thick rubber skin.

In order to be possible to fit a model in the wind tunnel testing facility the model has to be reduced to half size, meaning that the dimensions of the half wing in its retracted state become:

- 0.5m long span wise.
- 0.11m long chord wise.

Also, in order to reduce actuation forces needed to deform the wing skin, the skin thickness was reduced to 0.001m.

The wind tunnel model is assumed to increase span and chord in the same proportions of the full scale FEM model, which are 50% increase in span and chord dimensions. Therefore, the same stress levels on the skin must be caused by the mechanism.

For the normal stress in spanwise direction we have:

$$\sigma_{Fullscale} = \frac{F_{Fullscale}}{A_{Fullscale}} = \frac{F_{Fullscale}}{st_{Fullscale}sb_{Fullscale}} = \sigma_{Fullscale}$$

$$\frac{F_{Fullscale}}{st_{Fullscale}sb_{Fullscale}} = \frac{F_{Halfscale}}{\frac{st_{Fullscale}}{2}\frac{sb_{Fullscale}}{2}} \Rightarrow F_{Halfscale} = \frac{F_{Fullscale}}{4}$$

This means that the actuation forces in the half scale model with half skin thickness are four times smaller relative to the full size model. The same reasoning can be used for the stress in chord wise direction.

For the wing thickness direction forces, the reasoning is a little different since it depends on the wing sections relative thickness. Assuming the final relative thickness of the half scale wing is approximately the same as the full scale one, the compressive force in the thickness direction is reduced to half, due to the reduction to half of the skin thickness.

Therefore, for the dimensioning of the half scale wing model for wind tunnel testing is based on the

following actuation forces:

- Span extension maximum actuation force - 2000N.

- Chord extension maximum actuation force per rib - 375N.

- Skin maximum compression force in wing thickness direction- 125N.

Since the half scale wing dimensions are very small, the thickness of the wing sections does not allow the design of an economically and technically feasible airfoil morphing mechanism.

Because of this, the decision of actively changing the wing airfoil was discarded and only chord and span changes were considered for the morphing mechanism design.

Of course, changes in chord dimension change the airfoil shape, but the airfoil cannot be actively changed for a given chord length.



a)                                                     b)
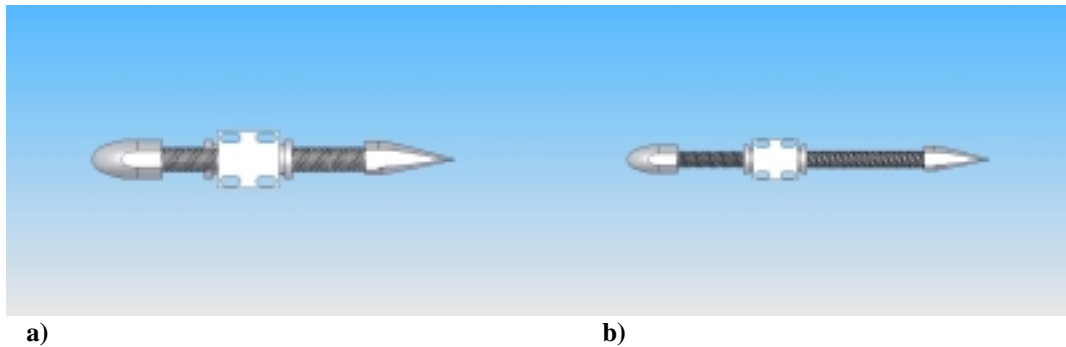
**Figure 7: Designed rib extension mechanism a) Retracted. b) Extended**

As can be seen in the pictures above, the airfoil at each rib will have three fixed shape sections which will change their relative position along the chord axis as the total chord changes.

All the other requirements and assumptions made for the full scale FEM modeling are taken into account in this new mechanism design:

Another requirement that was discarded at this time was the minimum weight one. Minimizing weight is of course very important in aerospace engineering but the main goal in this project is to prove if concept works or not, optimization of this model can be performed as future study after the concept is proved.

### 3.1.1 Mechanism Design

Some of the ideas for the morphing wing design explained in the previous chapter were used in this new design version, as the spar extension mechanism. The main differences would be in the chord expansion mechanism, since now it can be simpler because the requirement to actuate vertical screws to change the airfoil shape was dropped.

In this version, a fixed block in each rib supports the whole rib structure and connects the whole mechanism with the spars while screws make translation movements trough the block core and stretch the wing skin.

The block also supports the nuts which are mated to the screws and are the only moving parts of the rib, since they are rotationally actuated to cause the screws translation movement.
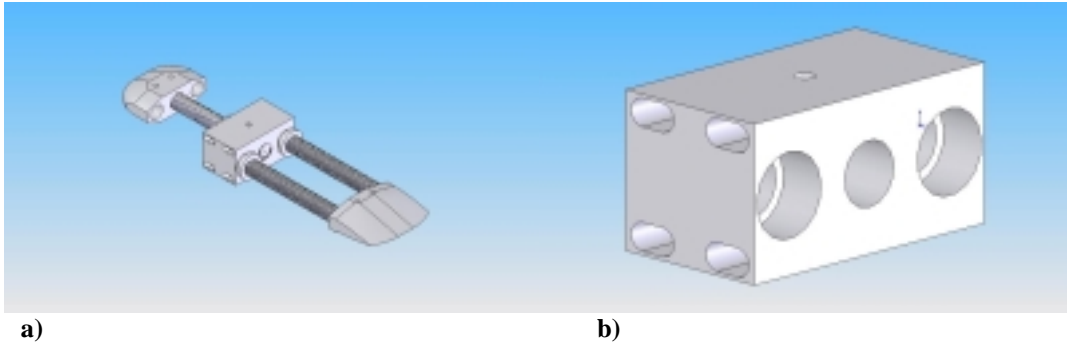


a)                                                                b)

**Figure 8: Rib Parts a) Assembled rib expansion mechanism. b) Central Block**

Attached to the tip of the screws there are the leading edge and trailing edge blocks. These blocks have the function of shaping the wing skin at the leading and trailing edge, respectively, and also serve as support for the leading and trailing edge shaping beams.



a)                                                                b)

c)                                                                d)
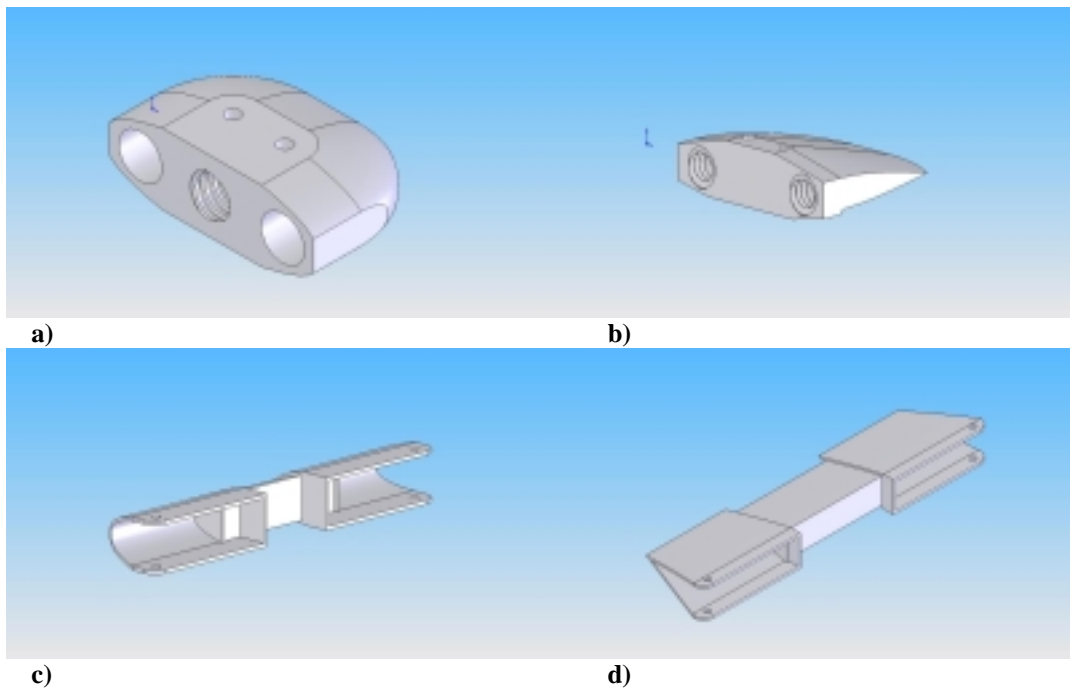
**Figure 9: Rib Parts a) Leading edge block. b) Trailing edge block. c) Leading edge shaping beams. d) Trailing edge shaping beams**

The function of these extendable beams is, as it happens with the leading and trailing edge blocks, is to maintain the leading and trailing edge shape in the wing sections between ribs.

The beams are connected to the leading and trailing edge block through hinges to allow the tapered form in the wing sections between ribs.
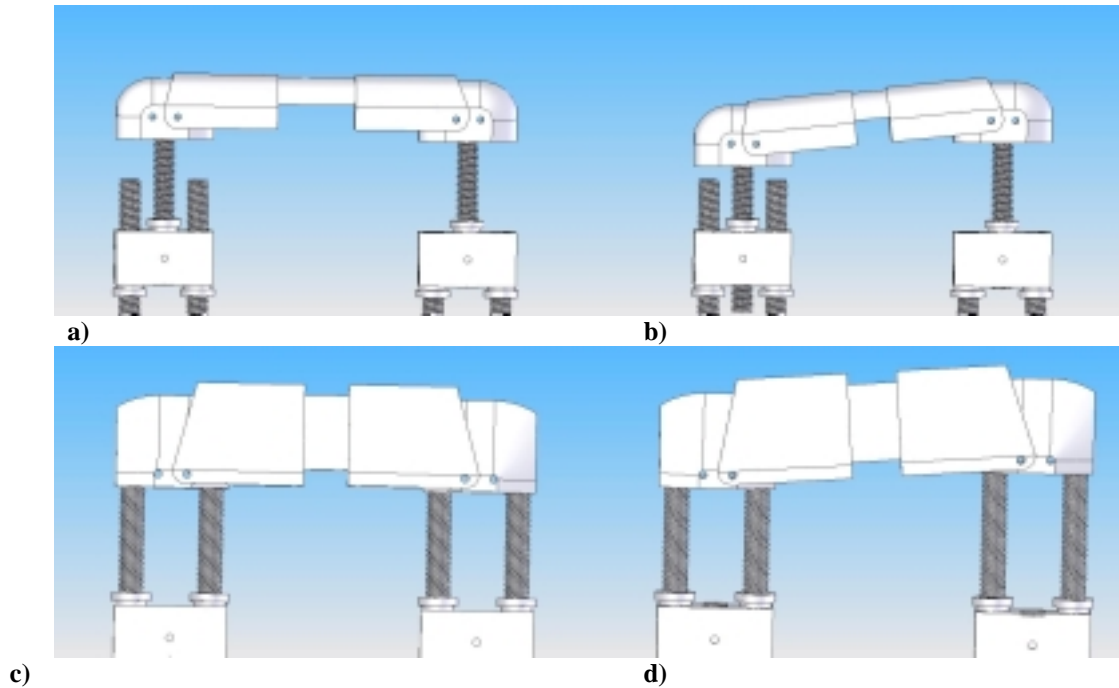
**Figure 10: Leading and trailing edge beams assembly with the rib expansion mechanisms a) Leading edge assembly straight. b) Leading edge assembly tapered. c) Trailing edge assembly straight. d) Trailing edge assembly tapered.**

With this design, each rib is actuated independently through the use of chains that rotate the screw nuts. This will allow greater freedom in obtaining the optimized wing planform shape, although it will increase wing weight. This is possible by using twelve electric motors attached to ribs, two per rib, and transmitting the motion with chains to the rotating nuts.

The span extension mechanism is based in beams that are pulled through the use of actuation, stretching the wing skin. The number of beams and their position is a function of the loading and dimensional constraints of the wing sections.

This mechanism also includes the hinged structure that places the ribs equally spaced along the span, as in the first version.
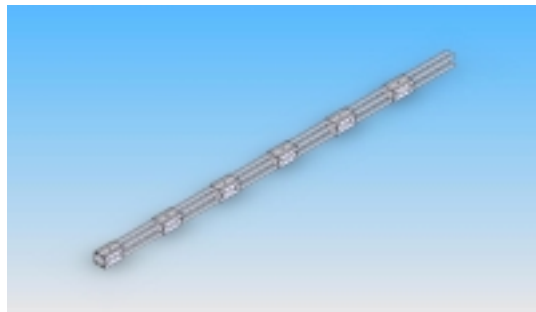


**Figure 11: Spar expansion mechanism**

In order to expand the wing span, the wing spars must be pushed in the spanwise direction. Therefore an actuation mechanism was designed based in screws, nuts and elastics. This mechanism ensures a uniform space between ribs by using elastics connecting them. Once they're the same, the same displacement will cause the same reaction force for all elastics that keeps the spacing.

It can be seen from figure 13 the mechanism assembly. The actuation plate pushes the spars and is supported by the threaded shafts that are fixed to the wing root plate with cross shape. The horizontal extensions of the root plate are used for clamping the wing skin.
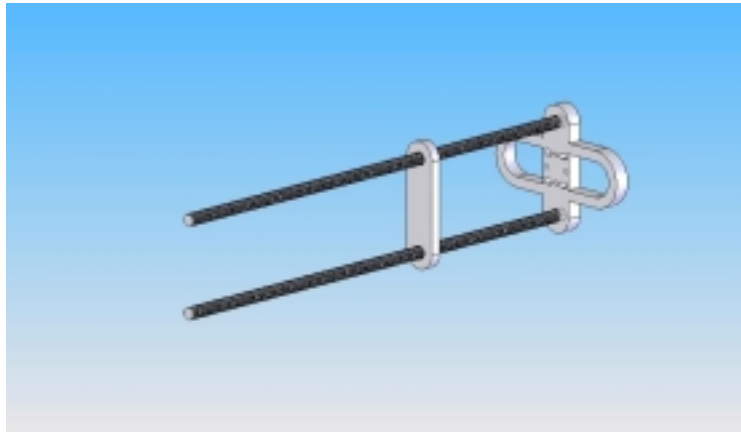


**Figure 12: Span expansion actuation mechanism**

The final mechanism assembly is shown in the next figure.
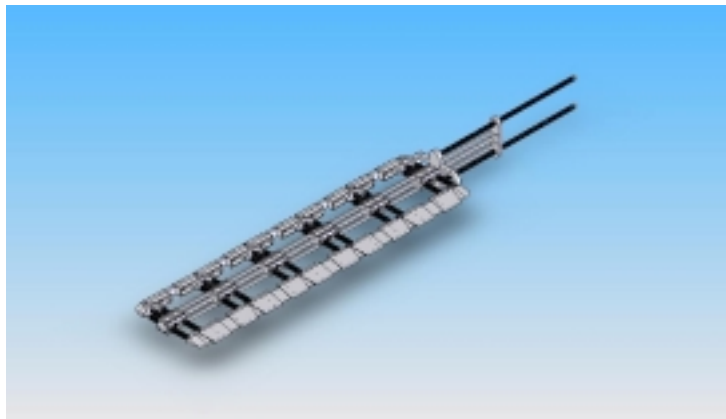


**Figure 13: Complete assembly of the morphing wing structure**

### 3.1.2 Mechanism Dimensioning

Spatial considerations are of the most importance due to the high forces involved and the small space available to fit the morphing mechanism that will support all the loads.

The first mechanism parts to be dimensioned are the critical ones that support direct loadings and produce the motion of the mechanism. Those parts include the rib threaded shafts, the spars and the spars actuation mechanism threaded shafts.

Other important parts are the tip, root and actuation plates, since they will be subject to the same loadings as the previous parts, although no buckling analysis is needed to dimension them. These parts were dimensioned and analyzed based only in FEM results to make sure the allowable stress was not exceeded.

The rotating rib nuts and the actuation mechanism nuts were dimensioned analytically. This dimensioning includes the necessary threaded length of the nuts to support the loadings and also the necessary nut thickness. FEM analysis was used to confirm stress levels on the nuts unthreaded thickness. Also the gearing of the nuts was dimensioned analytically.

The remaining parts (central block, leading edge and trailing edge blocks and beams) were dimensioned based on the wing geometry. Due to their higher dimensions FEM analysis was made only to confirm stress levels.

Finally, the pins that are used to connect some of the mechanism parts (leading and trailing edge blocks connect with the leading and trailing beams) are dimensioned to withstand pure shear in the connection surface.

No threads of the various threaded parts were included in any of the FEM analysis mentioned above.

Figure 14 shows the designed parts FEM meshes and loading and the stress results from FEM analysis.

| Material | E, GPa | v | $\sigma_{yield}$ Tension, MPa | $\sigma_{yield}$ Compression, MPa | $\tau_{ultimate}$, MPa |
|---|---|---|---|---|---|
| Aluminium | 72 | 0.33 | 345 | 345 | 283 |
| Steel | 200 | 0.3 | 345 | 345 | ---- |
| Acrylic | 2.2 | 0.3 | 47 | 100 | ---- |

**Table 3: Material Data**

### 3.1.2.1 Rib threaded shafts dimensioning

The rib shafts dimensioning was made based on the maximum actuation force per rib times a safety factor of 1.25 which gives the project loading of 469N of compressive force acting on a clamped shaft.

The material of the rib shafts was chosen to be aluminum with the characteristics shown on table 3 [17].

The critical shaft would be the leading edge shaft because it supports all the compressive loading alone

while the two trailing edge shafts support half the load each. Nevertheless the maximum length of the trailing edge shafts is higher and this is relevant for the buckling load calculation. Therefore, the shafts dimensioning took into account the maximum loading times the safety factor and the maximum shaft length, assuring structure stability in a conservative manner.

Analytical, linear FEM and nonlinear FEM analysis took place to calculate the buckling loads and stress on the rib threaded shafts. The analytical calculation is based on the following expression for the buckling load of a perfect column with a clamping support:

$$P_{cr} = \frac{EI\pi^2}{(2l)^2} \quad (1)$$

This expression is used for the other analytical critical load calculations in this section [18].

Results are shown on table 4.

### 3.1.2.2 Spars Dimensioning

The spars dimensioning was made based on the span wise actuation force times a safety factor of 1.25 which gives the project loading of 2500N of compressive force acting on a clamped beam.

The material of the spars was chosen to be steel with the characteristics shown on table 3.

A compromise between the available space and the necessary second moment of area to support the loading had to be made. Also the compressive loading is eccentric relative to the spars centroid when it reaches its maximum, since the spars geometrical centre is positioned at ¼ of the chord length from the leading edge.

Analytical, linear FEM and nonlinear FEM analysis were the methods used to calculate the buckling loads, stress and deformation due to the eccentric loading.

The choice made was for 8 small steel beams with 4mm diameter distributed inside the central block area. FEM analysis shows that the constraints on the beams displacement due to the rib blocks increase the critical load and prevent unallowable displacements.

Analytical calculation of the buckling load in the two principal directions was made without consideration for the eccentricity of the load. FEM nonlinear analysis was made using two models: one displaces the load from the spars centroid by a calculated amount and other including the skin material and forcing it to stretch in a similar way as the wing skin. This last analysis has shown the necessary skin deformation forces to be considerably lower than the project loading assumed.

Results are shown on table 4.

### 3.1.2.3 Spars actuation mechanism threaded shafts

These shafts are subject to tension and not compression as the previous ones, therefore simple stress calculation was made to determine the shaft inner diameter. Results are shown on table 4.

| Part | Material | Load, N | Diam. x Lengh, mm | $P_{cr}$ Euler, N | $P_{cr}$ Linear FEM, N | $\sigma_{VM}$, MPa |
|---|---|---|---|---|---|---|
| Rib Shaft | Aluminium | -489 | 7x96.25 | -2260.13 | -2258.98 | 93.6 |
| Spars (eccentric load) | Steel | -2000 | 4x750 | -3953.32 | -3133.80 | 335 |
| Spars (skin & spars non-linear FEM) | Steel | -1794 | 4x750 | ---- | ---- | 307 |
| Spars actuation shaft | Aluminium | 1250 | 6x330 | ---- | ---- | 44.2 |

**Table 4: Rib threaded shaft, spars actuation shafts dimensioning results**

### 3.1.2.4 Tip, root and actuation plates

Dimensioning these plates means dimensioning only the thickness of the plates in order to keep the stress level under the allowable value. Results are shown on table 5.

### 3.1.2.5 Rotating rib nut

The rotating rib nut has to be thick enough to withstand the compressive loading of the rib threaded shaft and also long enough so that the threaded length is enough to support the shear stress caused by the loaded shaft.

The calculation of the threaded length $(L_e)$ is based on the approximate formulas shown below [19].

$$\tau_{max} = \frac{F}{A_s} \qquad (2)$$

Where $\tau_{max}$ is the allowable shear stress for the nut material and $A_s$ is the shear resistive area of the nut. $A_s$ is given by (3).

$$A_s = \frac{\pi}{2} d_p L_e \quad (3)$$

Here $d_p$ is the pitch circle diameter of the thread and is given approximately by (4)

$$d_p = D - 0.64952 p \quad (4)$$

Thus, the minimum threaded length of the nut/screw is given by (5).

$$L_e = \frac{2F}{\pi(D - 0.64952 p)\tau_{max}} \qquad (5)$$

Although these formulas are approximate, they give conservative results.

FEM analysis was used to obtain the stress levels on the nut. Results are shown on table 6.

### 3.1.2.6 Actuation mechanism nuts

The dimensioning process of these nuts is based on the same assumption than the rotating rib nut, but with different loading, since these nuts support the spanwise loading of the structure.

FEM analysis was used to obtain the stress levels on the nut. Results are shown on table 6.

### 3.1.2.7 Central block, leading and trailing edge blocks and beams

These parts were analyzed using FEM. No unallowable stress level was found.

| Part | Material | Total Load, N | Thickness, mm | $\sigma_{VM}$, MPa |
|---|---|---|---|---|
| Tip Plate | Aluminium | 2500 | 4 | 194 |
| Root Plate | Aluminium | 2500 | 10 | 317 |
| Actuation Plate | Aluminium | 2500 | 5 | 270 |

**Table 5: Tip, root and actuation plates dimensioning results**

| Part | Material | Total Load, N | Thickness, mm | D, mm | p, mm | $L_e$, mm | $A_s$, mm$^2$ | $\tau$, MPa | $\sigma_{VM}$, MPa |
|---|---|---|---|---|---|---|---|---|---|
| Rotating rib nut | Aluminium | 489 | 1 | 9.24 | 2 | 9 | 113 | 4.15 | 33.6 |
| Actuation nut | Aluminium | 1250 | 3 | 15 | 5 | 10 | 145 | 8.61 | 14.9 |

**Table 6: Rotating rib and actuation nuts dimensioning results**

| Part | Material | Total Load, N | Thickness, mm | $\sigma_{VM}$, MPa |
|------|----------|---------------|---------------|--------------------|
| Central block | Acrylic | 489 | ---- | 14.4 |
| Leading edge block | Acrylic | 489 | ---- | 37.3 |
| Trailing edge block | Acrylic | 489 | ---- | 91.3 |
| Leading edge beams | Aluminium | 489 | 1 | 162 |
| Trailing edge beams | Aluminium | 489 | 1 | 129 |

**Table 7: Tip, root and actuation plates dimensioning results**

### 3.1.2.8 Connecting pins

These pins are dimensioned to withstand pure shear. Results are shown in table 8.

| Part | Material | Total Load, N | Diameter, mm | $\tau$, MPa |
|------|----------|---------------|--------------|-------------|
| Pin | Aluminium | 489 | 3 | 69.2 |

**Table 8: Rotating rib and actuation nuts dimensioning results**
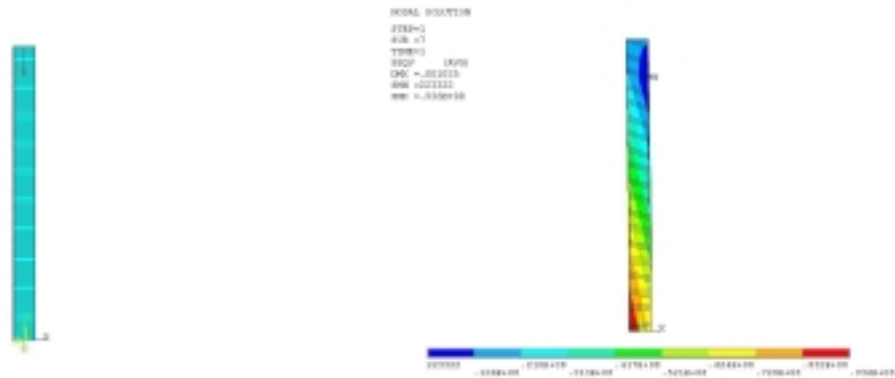


**a) Rib threaded shaft FEM mesh**

**b) Rib threaded shaft equivalent Von Mises stress**
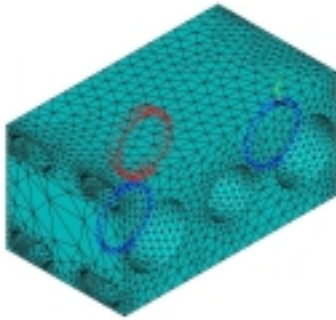
**c) Spar eccentrically loaded FEM mesh**
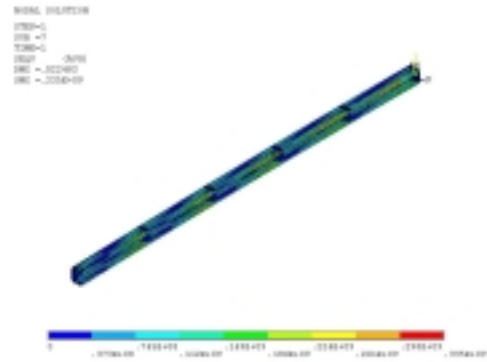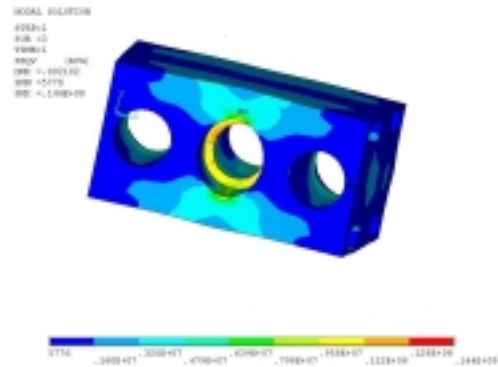


**d) Spar eccentrically loaded equivalent Von Mises stress**



**e) Spar and skin FEM mesh**
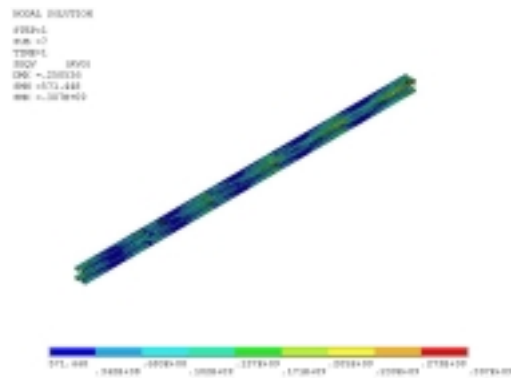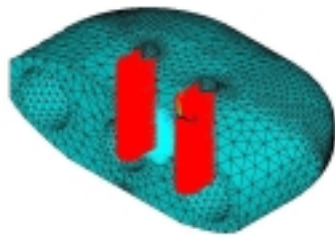


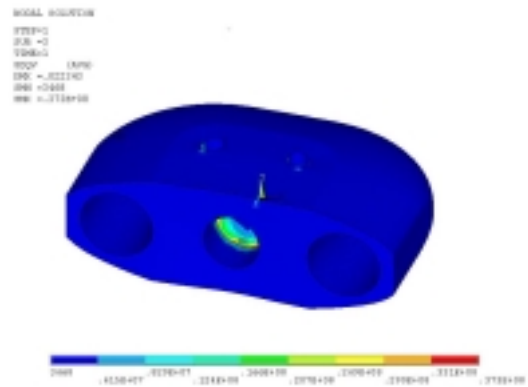**f) Spar equivalent Von Mises stress**



**g) Central block FEM mesh**



**h) Central block equivalent Von Mises stress**
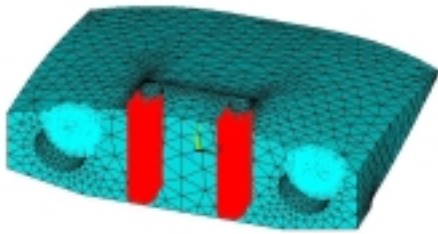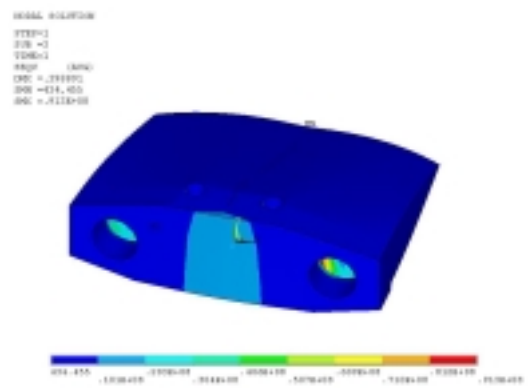
**i) Leading edge block FEM mesh**



**j) Leading edge block equivalent Von Mises stress**



**k) Trailing edge block FEM mesh**



**l) Trailing edge block equivalent Von Mises stress**

**Figure 14:  Morphing mechanism parts FEM meshes and stress results**

### 3.1.3 Actuation torque requirements

For the calculation of the actuation torque needed for rib and actuation nuts we calculate the torque needed to raise a load supported by a fastened screw. This calculation is based on the following expressions [20]:

$$M = F \frac{d_p}{2} \left[ \frac{\left( \cos\left( \frac{\theta_n}{2} \right) \tan(\beta) + f \right)}{\cos\left( \frac{\theta_n}{2} \right) - f \tan(\beta)} \right] + F R_m f' \qquad (6)$$

$$\frac{\theta_n}{2} = a\tan\left[ \tan\left( \frac{\theta}{2} \right) \cos(\beta) \right] \qquad (7)$$

$$\beta = a\tan\left( \frac{p}{\pi d_p} \right) \qquad (8)$$

The first term in (6) represents the necessary torque to overcome the friction between the threads of the

screw and nut while the second term represents the necessary torque to overcome the friction between the nut and the support surface where the nut lies on.

Expression (7) relates the angle between the reaction force and the axis of the screw with the screw parameters $\theta$ and $\beta$, where $\theta$ is the thread profile angle and $\beta$ is given by (8).

Results for the maximum torque are shown in table 9.

| Part | Material | Total Load, N | p, mm | $d_p$, mm | $\theta$, ° | f | f' | M, Nm |
|------|----------|---------------|-------|-----------|------------|---|----|-------|
| Rotating rib nut | Aluminium | 489 | 2 | 7.99 | 29 | 0.3 | 0.3 | 1.49 |
| Actuation nut | Aluminium | 1250 | 5 | 9.24 | 29 | 0.3 | 0.3 | 5.47 |

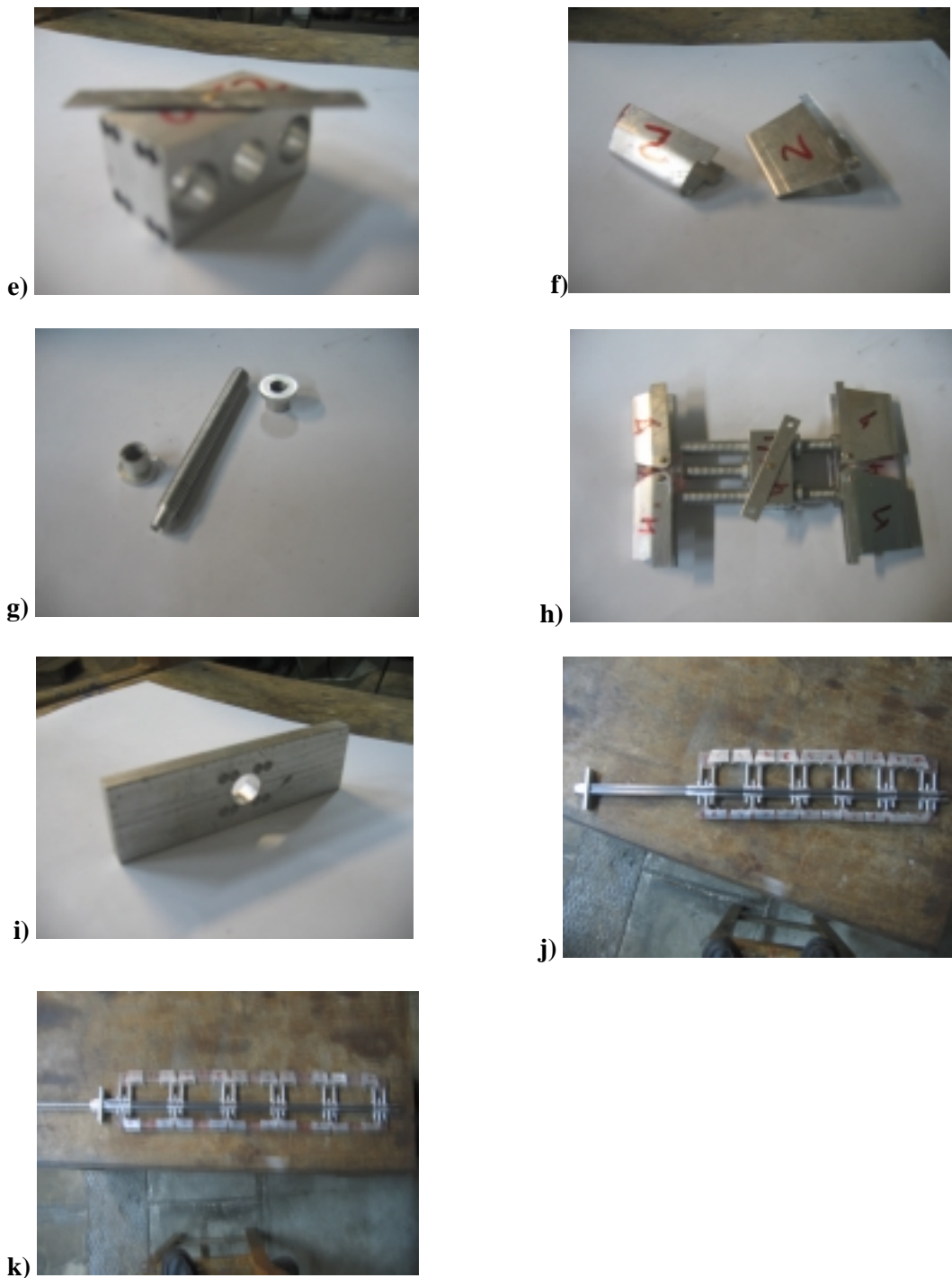**Table 9: Rotating rib and actuation nuts torque requirements**

## 3.2 Morphing wing prototype construction

The morphing wing prototype construction procedure tried to follow the mechanism design as close as possible given the available resources.

Figure 15 shows some of the different parts of the mechanism and the final assembly.



a)



b)



c)



d)

e)



f)



g)



h)



i)



j)



k)
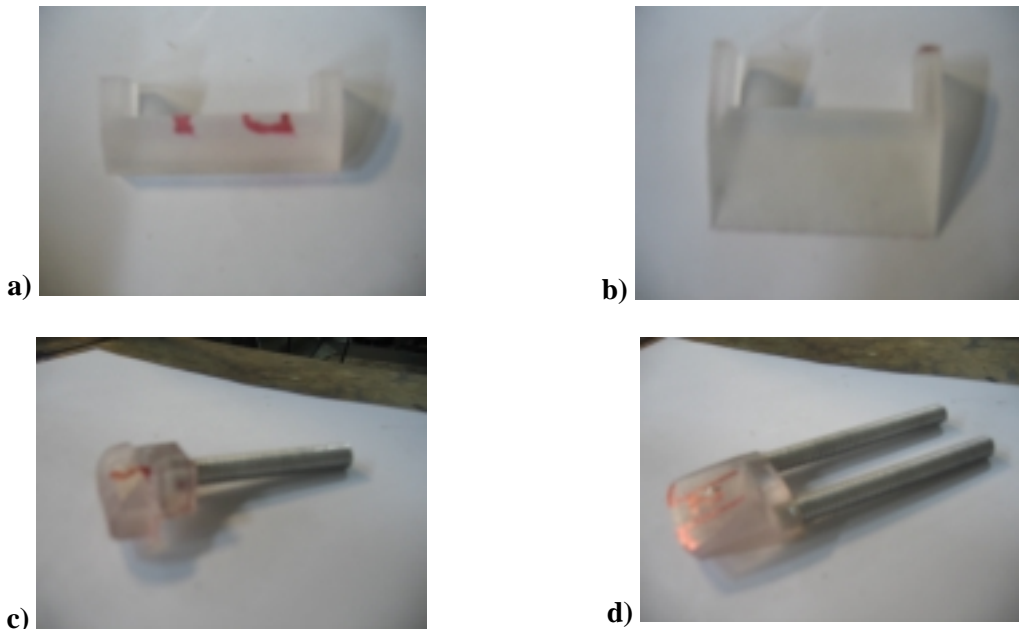
**Figure 15: Morphing Mechanism Parts a) Leading edge interior beam b)Trailing edge interior
beam c) Leading edge block and screw d) Trailing edge block and screw e) Central block f)
Leading and trailing edge exterior beams g) Rotating nuts and screw h) Chord extension
mechanism assembly  i) Span actuation mechanism plate j) Final mechanism assembly
(retracted) k) Final mechanism assembly (extended)**

Special concern was given to critical parts as the wing spars and the chord expansion screws, which were

built in a conservative way for the design loads. Nevertheless perfect alignment of the mechanism different parts was impossible to obtain.

This caused a decrease in the overall spars bending stiffness since they act as eight separate spars instead of a single spar, so bending caused by the wing's own weight is not negligible. The wing lift may contribute to the wing becoming straight spanwise.

Also torsional stiffness is affected. The wing is easily twisted and problems may arise from this fact. At the moment one possible solution is to add conformal plates to the upper and lower sides of the central blocks to prevent their rotation and act as a conformal element between ribs.

The span expansion mechanism proved to fail the intent of keeping the ribs equally spaced along the span. The gaps between the connecting pins and the small plates, along with alignment difficulties caused the structure to block due to friction. An alternative solution was implemented by using rubber strings connecting the central blocks along the span. If the rubber strings are similar, the ribs will be equally spaced along the span.



**Figure 16: Detail of the rubber strings in the final mechanism assembly**

Torque actuation requirements for the chord expansion mechanism are prohibitive for the small size of the wing, since the small actuators that fit in the available space in the wing can't produce a torque that high.

The solution was to substitute the wing skin material by a different kind of rubber like material, somewhat less stiff, reducing this way the loads in the chord expansion mechanism and the wing spars. For that purpose a new composite material was built. It was made of licra fibre inserted into a silicone matrix. The silicone matrix turns the licra fibre cloth impermeable to air and give the manufacturer control of the required deformation forces and thus the actuation torque. This is done by increasing or decreasing either the silicone matrix thickness or the number of layers of the licra fibre cloth, or both.

Possible drawbacks of implementing this solution are the decrease in overall wing rigidity and increase in wing skin deformation because of the aerodynamic loading.

## 4. WIND TUNNEL EXPERIMENTAL PROCEDURE AND MORPHING WING TEST RESULTS

At present the time wind tunnel testing procedure is under study. The fact that the wing skin is flexible and

needs to be stretched prevents the use of the wind tunnel scale without adaptations. Normally for a rigid wing a small scale prototype of the whole wing would be tested and connected to the scale by a support at the semi span of the wing.

In our research only a half wing prototype was built to allow the span increase actuation mechanism to be actuated manually and avoid the aerodynamic drag caused by it. Note that this mechanism would be inside the fuselage and so it wouldn't contribute to wing drag.

The wing support is being built and experimental results will be available soon.

# 5. REFERENCES

[1] M. Abdulrahim and J. Cocquyt, "Development of Mission Capable Flexible Wing Micro Air Vehicles", University of Florida, Gainesville, FL 32611-6250, 2002.

[2] Mujahid Abdulrahim and Rick Lind, "Flight Testing and Response Characteristics of a Variable Gull-wing Morphing Aircraft", University of Florida, 2004.

[3] Mujahid Abdulrahim, "Flight Dynamics and Control of an Aircraft with Segmented Control Surfaces", University of Florida, AIAA-RSC2-2003-U-010.

[4] Justin Edward Manzo, "Analysis and Design of a Hyper Elliptical Cambered Span Morphing Aircraft Wing", Cornell University, 2006.

[5] David Cadogan, Tim Smith, Frank Uhelsky and Matt MacKusick, "Morphing Inflatable Wing Development for Compact Package Unmanned Aerial Vehicles", AIAA2004-1807, 2004.

[6] E. Forster B. Sanders, F. E. Eastep, "Aerodynamic and Aeroelastic Characteristics of Wings with Conformal Control Surfaces for Morphing Aircraft", Journal of Aircraft 40, no. 1.

[7] P.Bourdin, A.Gatto and M.I. Friswell, "The Application of Variable Cant Angle Winglets for Morphing Aircraft Control", University of Bristol, AIAA2006-3660, 2006.

[8] Bae, J. , Seigler, T., Inman, D., "Aerodynamic and Aeroelastic Considerations of A Variable-Span Morphing Wing", 45th AIAA/ASME/ASCE/AHS/ASC Structures, Structural Dynamics & Materials Conference, 19 - 22 April 2004, Palm Springs, California

[9] Secanell, M., Suleman, A., Gamboa, P., "Design of a Morphing Airfoil Using Aerodynamic Shape Optimization", AIAA Journal, Vol. 44, No. 7, July 2006, pp. 1550-1562.

[10] Moniz, P. A. A., "Adaptive Aeroelastic Aircraft Structures", PhD Thesis, Instituto Superior Tecnico, Universidade Tecnica de Lisboa, Lisbon, 2005.

[11] Vale, J., Lau, F., Suleman, A., and Gamboa, P., "Multidisciplinary Design Optimization of a Morphing Wing for an Experimental UAV", 11th AIAA/ISSMO Multidisciplinary Analysis and Optimization Conference, Portsmouth, Virginia, USA, 6-8 September, 2006.

[12] Drela, M., *XFOIL 6.94 User Guide*, MIT Aero & Astro Harold Youngren, Aerocraft, Inc., 10 December 2001.

[13] Anderson, J. D., Corda, S., and Wie, D. M. V., "Numerical Lifting Line Theory Applied to Drooped Leading-Edge Wings Below and Above Stall," *Journal of Aircraft*, Vol. 17, No. 12, 1980, pp. 898-

904.

[14] Spellucci, P., *DONLP2 Users Manual*, Department of Mathematics, Technical University at Darmstadt.

[15] ANSYS, Inc. Ansys® Release 8.0 Theory - Reference.Guide.

[16] PlymerFEM, http://polymerfem.com/modules.php?name=Materials_Models&material=8, March 2007

[17] Material Property Data, http://www.matweb.com, March 2007

[18] Engineering Fundamentals, http://www.efunda.com, March 2007

[19] http://www.roymech.co.uk, March 2007

[20] Shigley, J. E. and Mischke, C. R., *Mechanical Engineering Design*, 7th ed., McGraw Hill, 2003.